Nanoscale

Atomically Sharp Interlayer Stacking Shifts at Anti-phase Grain Boundaries in Overlapping MoS2 Secondary layers

SCHOLARONE™
Manuscripts

Atomically Sharp Interlayer Stacking Shifts at Anti-phase Grain Boundaries in Overlapping MoS$_2$ Secondary layers

Si Zhou[1], Shanshan Wang[1,2], Zhe Shi[3], Hidetaka Sawada[4], Angus I. Kirkland[1,5], Ju Li[3,6], Jamie H. Warner[1]*

[1]Department of Materials, University of Oxford, 16 Parks Road, Oxford, OX1 3PH, United Kingdom

[2]Science and Technology on Advanced Ceramic Fibers & Composites Laboratory, National University of Defense Technology, Changsha 410073, Hunan Province, China

[3]Department of Materials Science and Engineering, MIT, 77 Massachusetts Ave, Cambridge, MA 02139, USA

[4]JEOL Ltd., 3-1-2 Musashino, Akishima, Tokyo 196-8558, Japan

[5]Electron Physical Sciences Imaging Center, Diamond Light Source Ltd, Didcot, UK

[6]Department of Nuclear Science and Engineering, MIT, 77 Massachusetts Ave, Cambridge, MA 02139, USA

Email: *Jamie.warner@materials.ox.ac.uk

Abstract

When secondary domains nucleate and grow on the surface of monolayer MoS$_2$, they can extend across grain boundaries in the underlying monolayer MoS$_2$ and form overlapping sections. We present an atomic level study of overlapping anti-phase grain boundaries (GBs) in MoS$_2$ monolayer-bilayers using

1

aberration-corrected annular dark field scanning transmission electron microscopy. In particular we focus on the antiphase GB within a monolayer and track its propagation through an overlapping bilayer domain. We show that this leads to an atomically sharp interface between 2H and 3R interlayer stacking in the bilayer region. We have studied the micro-nanoscale "meandering" of the antiphase GB in MoS_2, which shows a directional dependence on the density of 4 and 8 member ring defects, as well as sharp turning angles 90° ~100° that are mediated by a special 8-member ring defect. Density functional theory has been used to explore the overlapping interlayer stacking around the antiphase GBs, confirming our experimental findings. These results show that overlapping secondary bilayer MoS_2 domains cause atomic structure modification to underlying anti-phase GB sites to accommodate the van der Waals interactions.

KEYWORDS: ADF-STEM, antiphase boundary, MoS_2 bilayer, 2D materials

Introduction

MoS_2 is a semiconducting transition metal dichalcogenide (TMD) with a direct band gap in monolayer form, and indirect in the bulk.[1-4] It offers a band gap in the red visible spectrum and semiconducting properties that expand the applications for 2D materials beyond what graphene can achieve.[5-7] Moreover, large-area monolayer MoS_2 can be synthesized using CVD[8-11], making it a promising candidate for building atomically thin, layered electrical, optical, and photovoltaic devices.[12-16] However, in the production of large-area 2D materials, grain boundaries (GBs) are inevitably produced between randomly oriented crystal domains within a polycrystalline film.[17-19]

Conventional GBs in 3D polycrystalline and nanocrystalline solids influence their mechanical, physical and chemical properties.[20,21] The general effects of GBs on the properties of 2D materials can be assigned to GB dislocation cores, the orientation mismatch between grains and the in-plane and out-

of-plane strains introduced.[22] GBs in graphene are usually formed by dislocation cores consisting of pentagon-heptagon ring pairs.[23-25] The presence of GBs can also lead to detrimental effects on some properties of graphene, including reduced electron mobility,[26-29] thermal conductivity,[30] and reduced ultimate mechanical strength.[31] Conversely, GBs in graphene can also be beneficially exploited via controlled GB engineering.[32]

Recently, GBs have been shown to play an important role in reducing the charge carrier mobility in monolayer MoS_2.[33] These extended defects can act as undesired sinks for carriers, increasing their scattering and degrading electrical performance.[34-35] Individual GBs can also strongly affect the photoluminescence of MoS_2 monolayers and alter their in-plane electrical conductivity.[36] All of these effects strongly depend on the GB tilt angles and the local doping and strain introduced by dislocation cores.[36] Therefore, atomic structure analysis of these GBs can facilitate tailoring the properties of MoS_2 via controlled defect engineering. Dislocation cores in monolayer MoS_2 vary in configuration due to the Mo-S bonding characteristics. Structures including 5-7, 4-4, 4-6, 6-8 and 4-8 rings are both theoretically predicted and have been experimentally observed,[36-41] and are dependent on the local Mo/S source concentration as well as the tilt angle.[37] Furthermore, the misorientation angle of the tilt GB ranges from 0° to 60° due to the 3-fold symmetry of MoS_2 lattice.[36-41]

The 60° GBs (also denoted as antiphase boundaries), are of particular interest as they form one-dimensional metallic wires in a semiconducting MoS_2 matrix,[36-39,41,42] and act as conductive channels that have a profound influence on both transport properties and exciton behavior of the monolayers.[37,38,43] Experimental studies have shown that a single 60° GB can enhance the in-plane electrical conductivity and substantially quench the local photoluminescence.[44] Structural studies at atomic resolution have revealed that these GBs introduce mirror symmetry between two grains, which

are connected predominantly through lines of 8- and 4-membered rings.[37] Inversion domains surrounded by these 60° GBs are formed by annealing TMD monolayers at high temperature.[39] However, the micronanoscale distribution of the defects in antiphase GBs and their correlation to the propagation direction of the GB has yet to be studied in sufficient detail to gain an overall picture of their behavior. Furthermore, the nanoscale-microscale density and distribution of 4- and 8-rings associated with specific directions in the antiphase GB with atomic level detail has not been fully clarified. A few studies have described the growth mechanisms of grain boundaries in MoS_2 and graphene.[39,44-46] Studies of monolayer h-BN have shown that in polycrystalline regions two merging domains can have overlapping interface rather than atomically bonded.[47] Recent work has used ADF-STEM to study the strain maps around mirror twin grain boundaries in $MoSe_2$ bilayers with small grain boundaries and inversion domains, revealing strain relaxation within the local GB area.[48] However, the understanding of the behavior of GBs in monolayer-bilayer stacks on a larger size scale with dimensions extending to micron distances has yet to be explored in detail.

In this study, MoS_2 samples were grown on Si substrates with a 300nm oxide layer using methods previously described.[49] The samples of MoS_2 produced were predominantly monolayer, with occasional small bilayer domains on top of the larger monolayer film. We used annular dark field scanning transmission electron microscopy (ADF-STEM) to probe the atomic structure of antiphase boundaries in both MoS_2 monolayers and bilayers and have studied the 4-ring and 8-ring defects and their relationship with the meandering GB. We have also studied how an antiphase GB propagates from a monolayer to a an overlapping bilayer domain leading to modification of the 2H and 3R bilayer stacking configurations and possible growth processes for differently orientated antiphase boundaries in MoS_2 monolayers are discussed. Density functional theory (DFT) calculations have been used to provide

accurate model structures for multislice image simulations for comparison with the experimental ADF-STEM images in order to understand the impact of van der Waals forces.

Results and Discussion

Figure 1a shows a schematic illustration of how two rotated monolayer MoS_2 grains (A and B) can meet to form a tilt grain boundary, as highlighted red in the second panel. A secondary MoS_2 layer (C) nucleates on top of grain B and then continues growing to finally overlap across the top of grain A. This should lead to a GB section where one side has well defined stacking of 2H or 3R, and the other side has a Moire pattern with the orientation mismatch corresponding to the GB tilt angle. The low magnification ADF-STEM image in Figure 1b shows a region where a secondary MoS_2 domain has grown across a tilt GB in the underlying monolayer. Figure 1c shows the ADF-STEM image of the tilt GB in the monolayer MoS_2, taken from the red boxed area in figure 1(a), revealing a 17° tilt angle, figure 1(d). The bright nanoparticles in figure 1b are Pt and were intentionally deposited to help locate the GB regions easily in ADF-STEM. The ADF-STEM image in figure 1e shows the overlapping bilayer MoS2 region, with the green line indicating the GB position. Figures 1f, g shows the atomically resolved ADF-STEM images of the GB in the overlapping region, with 3R stacking at the top and Moire pattern below. This establishes that bilayer domains can grow across GBs that already exist in monolayer MoS_2. We now focus the rest of our study to anti-phase GBs, examining overlapping bilayer regions at antiphase GBs, as well as the nanoscale structure of anti-phase GBs in monolayers.
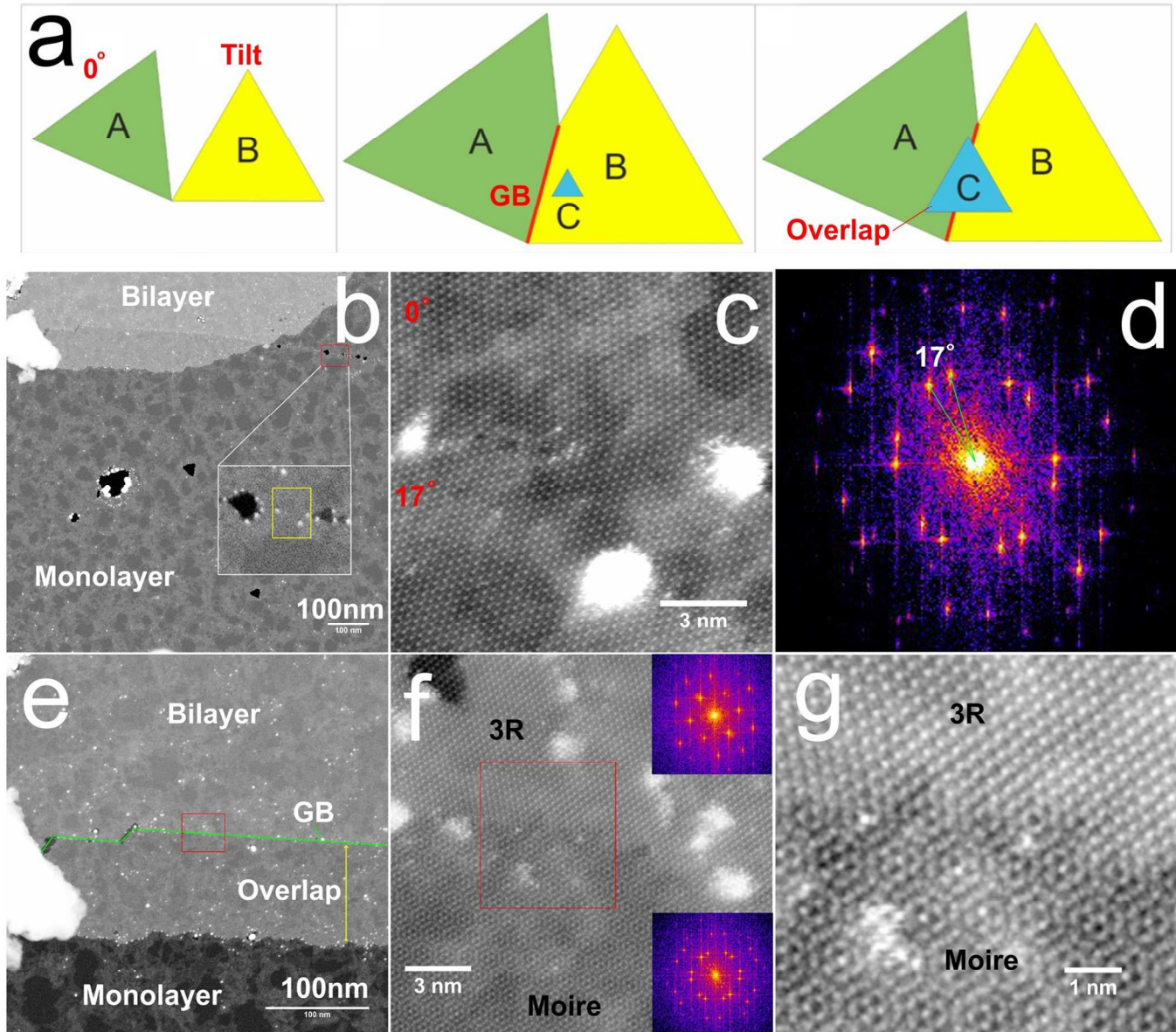
Figure 1. (a) Schematic illustrations showing how a secondary MoS$_2$ layer C grows across the GB between two rotated grains A and B, forming the overlapping bilayer GB region. (b) ADF-STEM image of a tilted GB in a monolayer MoS$_2$ region with an overlapping bilayer section. White box inset shows the magnified view from the red box area. (c) ADF-STEM image from the yellow boxed region in (b) showing the tilted GB (17°) in the monolayer MoS$_2$. The three Pt nanoparticles are seen as reference points. (d) FFT power spectrum from (c) showing the two sets of spots, giving tilt angle of ~17°. (e) ADF-STEM image showing the overlapping GB area from (b), with the GB indicated by the green line. (f) ADF-STEM image from the red box area in (e) showing the

overlapping bilayer GB has 3R stacking on its nucleation side (top) and Moire pattern on the overlapping side (bottom). Insets show FFT power spectra from each side of the GB in the image with 17° mismatch within the two layers comprising the Moire pattern, correlating to the tilt angle. (g) Higher magnification ADF-STEM image from the red box area in (f).

The schematic in Figure 2a, shows a secondary layer (C) growing on top of grain (B), which meets a 60° rotated grain (A) forming a grain boundary highlighted in red. Layer (C) approaches the GB during growth (Figure 2b) and finally reaches and grows across the GB (Figure 2c). Figure 2d shows the atomic model of the secondary layer on top of both grain A and B corresponding to Figure 2c which demonstrates that the GB is an antiphase GB, which introduces a 60° lattice rotation in the monolayer region (Figure 2e). The bilayer region exhibits a 2H-3R stacking sequence with the antiphase boundary at the interface between these. Hence, a stacking sequence change is predicted when the secondary layer grows across the antiphase boundary. The SEM image in Figure 2f shows several secondary layers grown on top of the GB (indicated by yellow dashed circles). The secondary layers are seen by their increased contrast in the SEM image and are also found in regions where grain boundaries are expected to form at the mirror plane between two merging single crystal domains.[50] A low magnification ADF-STEM image over a large field of view of a region is shown in Figure 2g and 2h, showing an antiphase GB in MoS_2 that exists within the larger monolayer that also propagates through regions containing bilayers (zone C and E). The mono-bilayer interface at zone B is magnified in Figure 2i. Pt nanoparticles were formed at the GBs during the TEM sample preparation stage to help find the GB location at lower magnification, but do not impact the results of the interlayer stacking structure presented in this work.[51] In the bilayer region, both 2H and 3R stacking sequences are observed with the antiphase GB at the interface. Magnified images at zone A and C are displayed in Figure 2j and k, respectively. Figure 2j shows octagonal and quadrangular configurations as the structural building blocks of the antiphase

boundary in monolayer. The same dislocation cores in bilayer region lead to sharp stacking transition

from 2H to 3R in Figure 2k. Schematic in Figure 2l demonstrates that the 4-member ring embedded in

the bottom layer of a bilayer system has more significant in-plane contraction, contributing to perfect
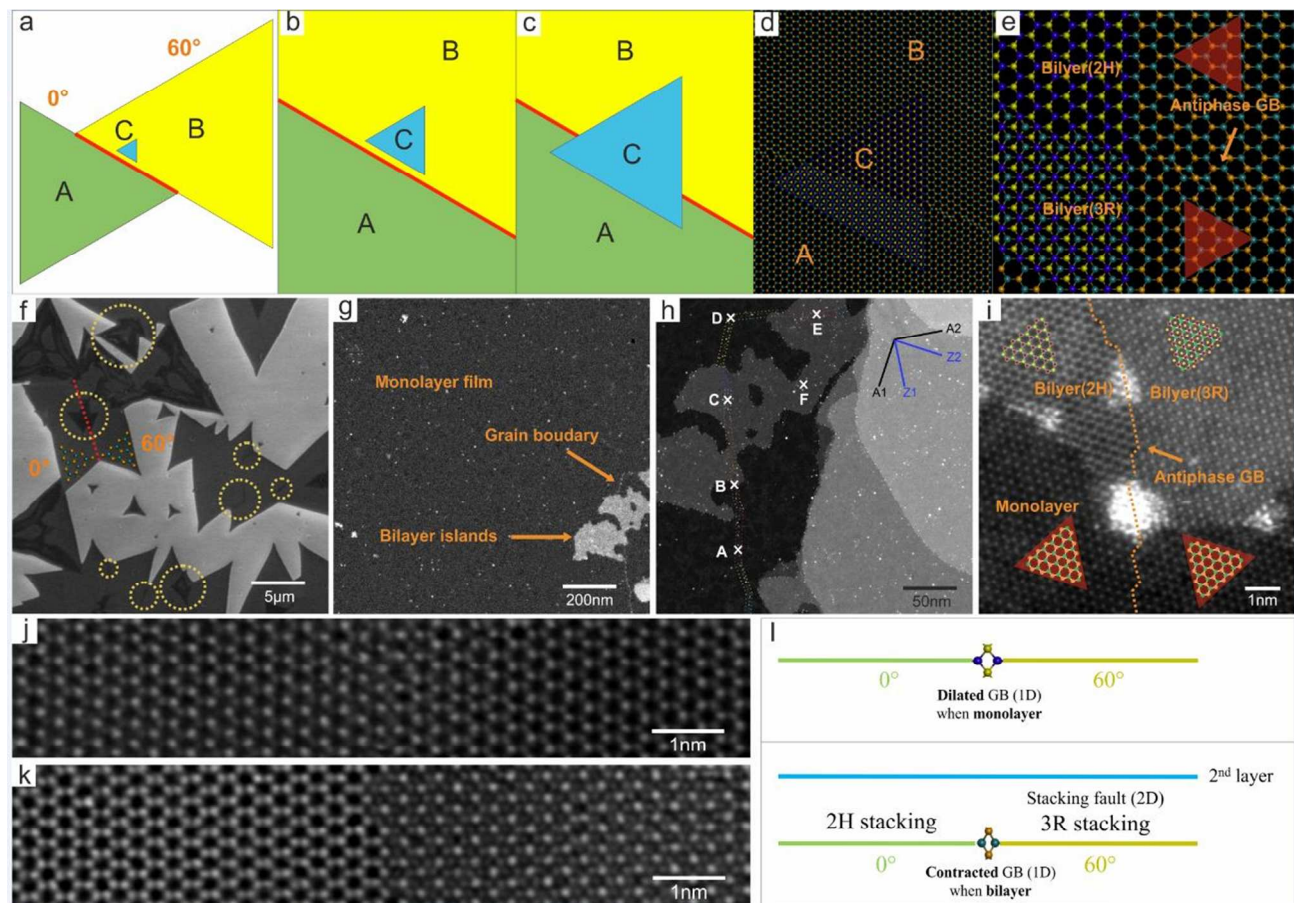
stacking sequences.

Figure 2. (a-c) Schematics showing a secondary MoS_2 layer C growing across the GB between two 60° rotated

grains A and B. (d) Atomic model based on the schematic in c. (e) Magnified image of the model showing the

antiphase GB in both monolayer and bilayer regions. (f) SEM image of several secondary layers grown on top of

GBs, one of which is formed between two 60° rotated grains as indicated. (g) Low magnification ADF-STEM

image of continuous monolayer MoS_2 with scattered bilayer islands suspended on holey SiN TEM grid. (h)

Intermediate magnification ADF-STEM image showing the propagation of a GB through monolayer and bilayer

regions. Zones along the pathway of the GB are marked as A-F. A1, A2, Z1 and Z2 represent armchair and zigzag directions. (i) ADF-STEM image of the GB in both monolayer and bilayer regions. Overlaid lattice diagrams show a 60° rotation for the monolayer grains and different stacking sequences in the bilayers. (j and k) Magnified images of zone A and C, respectively. (i) Schematics showing the contraction difference between the 4-member rings in monolayer and bilayer systems.

Higher magnification ADF-STEM images of Zone A and C with the antiphase boundaries are shown in Figures 3a and d, respectively. In the monolayer region, the antiphase GB introduces a mirror symmetric domain rotated by 60° with respect to the original lattice and in which the Mo and S sites are swapped. The overlaid atomic structure in Figure 3b indicates that the antiphase domains are joined by edge-sharing 4- and 8-member rings, similar to prior reports on MoS_2 GBs.[36] For the 4-member ring structure, Mo atoms retain 6-fold coordination whereas the S atoms change from 3-fold to 4-fold coordination changing the local stoichiometry from MoS_2 to Mo_4S_6 along the antiphase GB.[36] For the bilayer system, superimposed atomic structures shown in Figure 3e reveal two distinct stacking sequences denoted as 2H and 3R when one layer is overlaid on the other layer including the antiphase GB. The 4-member ring retains its configuration, whereas the 8-membered core appears as 6-4-4 motif in projection due to the 3R stacking sequence on the right-hand side of the boundary. The 4-member rings in both monolayer and bilayer regions are compared in detail in Figures 3c and f. The S-S and Mo-Mo (monolayer) or (Mo-2S)-(Mo-2S) and (2S-Mo)-Mo (bilayer) column distances were using boxed intensity profiles along the zigzag (A and C) and armchair (B and D) directions. Average values were obtained through multiple measurements from different regions. Due to the lattice distortion along these two directions in our experimental images (Figure S2), the distance measurement was normalized using the pristine MoS_2 lattice parameter as a reference. Within the 4-member ring in the monolayer, the S column distances

show similar values (3.13Å vs 3.18Å), whereas a ~24% shrinkage in Mo column distances is observed in the bilayer.
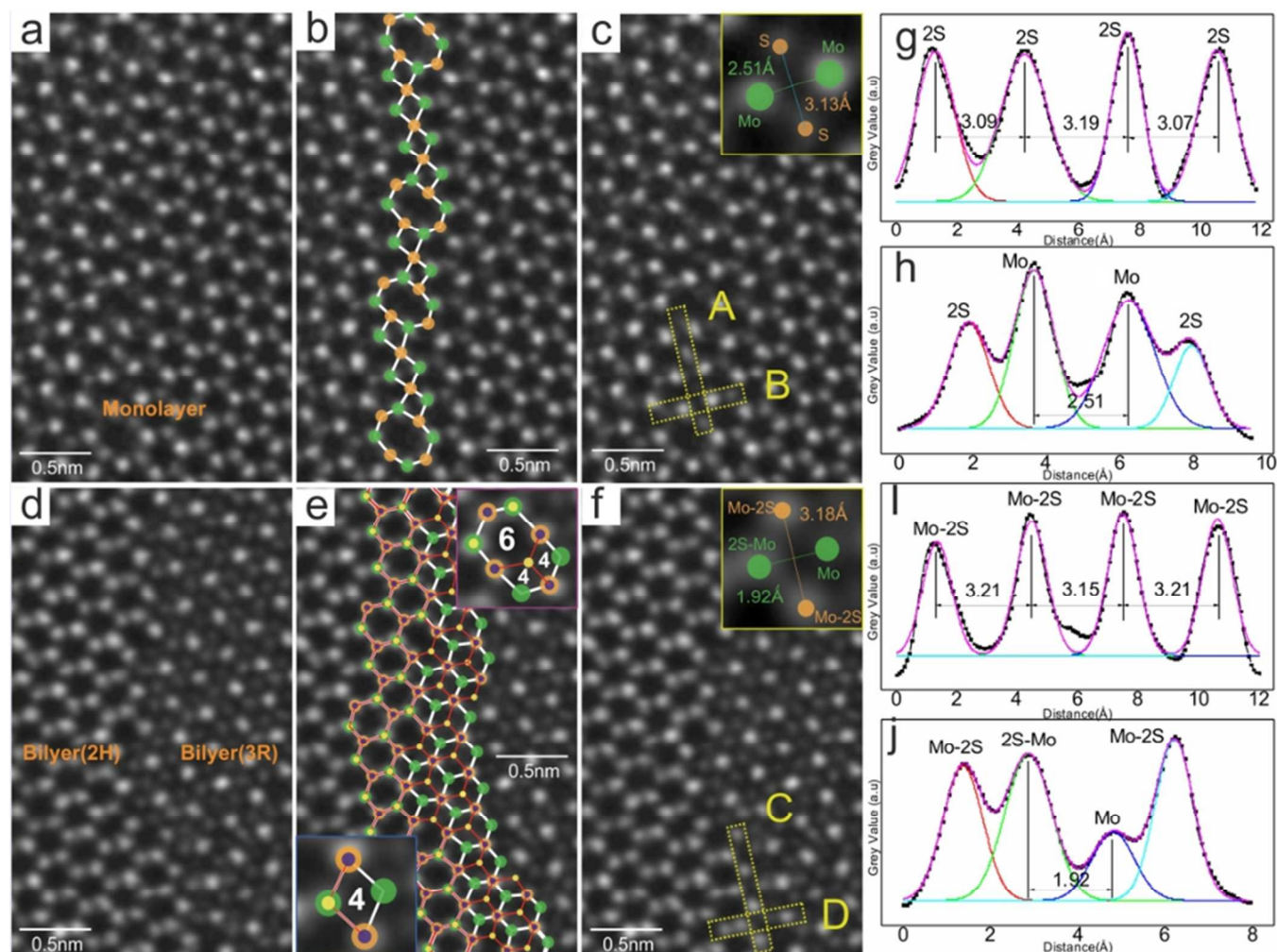

Figure 3. (a) ADF-STEM image of an antiphase GB in monolayer MoS_2. (b) The same region with the atomic structure overlaid. (c) The region shown in (a) with an inset showing the column distances in a 4-member ring. (d) ADF-STEM image of an antiphase GB in bilayer MoS_2. (e) The same region with the atomic structure and insets showing the dislocation core structure. The inset shows the column distances in a 4-member ring. (f) The region shown in (e) with an inset showing the column distances in a 4-member ring. (g-j) Boxed line intensity profiles taken along the directions A-D, respectively. Regions indicated by yellow boxed areas in (c) and (f). All distances are normalized by the lattice parameters of pristine MoS_2 monolayers.

To further study the reduction of the Mo-Mo distance in the 4-member rings, DFT calculations of both monolayer and bilayer MoS_2 systems were performed with a 4-4 chain along the zigzag direction as shown in Figure 4. A multislice image simulation based on the DFT relaxed model of the bilayer system is shown in Figure 4d and compared with our experimental image (Figure 4c). Boxed line intensity profiles were taken along direction 1 and 2 in both simulated and experimental images, and show excellent agreement. These results confirm that the antiphase boundary defects in the bottom layer lead to the atomically sharp transition between 2H and 3R stacking sequences. Figures 4a and 4b compare the antiphase GB structure in the bottom layer of a bilayer and a monolayer, respectively. Insets in Figure 4a and 4b show the bond lengths, indicating negligible difference in S-S column distances but a large discrepancy in Mo-Mo column distances (2.25Å for the monolayer and 1.85Å for the bilayer corresponding to a shrinkage of ~ 22%), which is similar to our experimental observations. Similar phenomena have been reported in monolayer graphene, where a ridge structure was found to separate fcc and hcp domains of a graphene/Ni(111) interface.[52] This bulging of graphene from the Ni(111) substrate facilitates matching of these two stacking sequences in a continuous film without any topological defects. In our case, this local in-plane compression perpendicular to the antiphase GB enables matching of the 2H and 3R stacking without any large out-of-plane distortion.
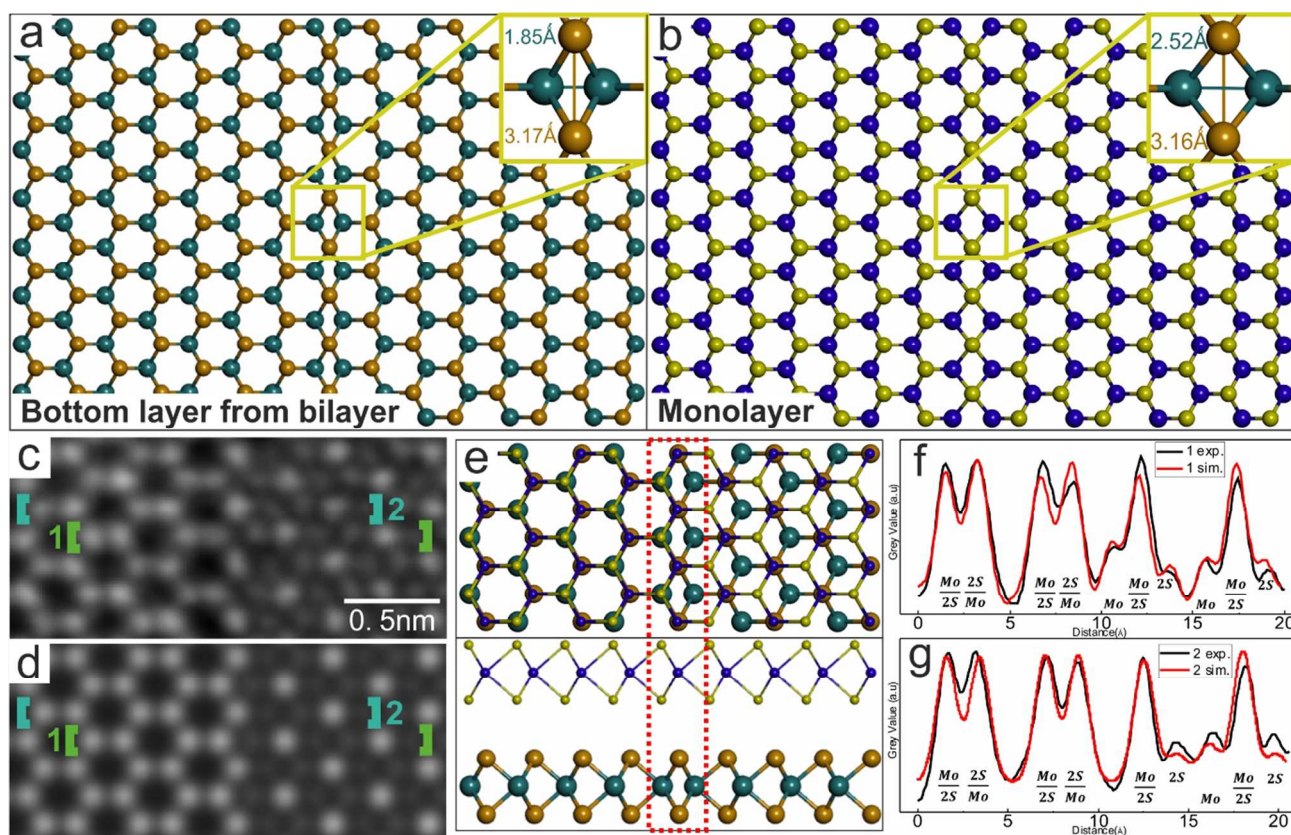
Figure 4. DFT-relaxed models of a monolayer antiphase GB (a) extracted from a bilayer and (b) from a pure monolayer. The insets show the column distances in the 4-member rings. (c) ADF-STEM image of a bilayer region with an atomically sharp 2H-3R stacking interface from the antiphase GB in one layer. (d) Multislice image simulation based on the atomic arrangement calculated in (e) from the DFT-relaxed model. The position of 4-member defects is highlighted in red. (f and g) Boxed intensity line profiles taken from (c) experimental and (d) simulated images along the directions marked 1 and 2, respectively. Widths of boxes are indicated by the brackets in (c) and (d).

Figure 5a shows a long section of the antiphase GB in a monolayer with different directions. The propagation direction of each segment is tilted from the zigzag direction by an angle θ, which ranges from 6.4° to 21.5° (as shown in Figures 5b to e). The defects are highlighted in each segment and their numbers are shown in Figure 5f. The 4-member rings outnumber the 8-member rings in all segments,

and the ratio (N8/N4) is as low as 0.33 for Figure 5b and as high as 0.51 in Figure 5e. The ratio (N8/N4) as a function of θ (Figure 5g) shows increased octagonal ring density with increasing θ. At the atomic level, 4-member rings provide GB propagation along the zigzag direction, whereas the 8-member rings provide arm-chair propagation, and the combination of these determines the arbitrary direction propagation. The ratio would equal 0 and 1 respectively if the GB propagated along the zigzag ($\theta = 0^{\circ}$) and the armchair direction ($\theta = 30^{\circ}$), respectively. Antiphase GBs act as 1D metallic wires embedded in the semiconducting MoS_2 matrix and kinks induce significant changes to the electronic behavior of a GB.[37] Alternatively, an antiphase GB has been reported to be n-doped due to the local Mo-rich environment arising from 4-member rings.[36,37] The n-doped GB shows significant PL quenching due to an increased electron density,[36] suggesting that lower PL intensity quenching could be achieved with a higher 8-member ring density.
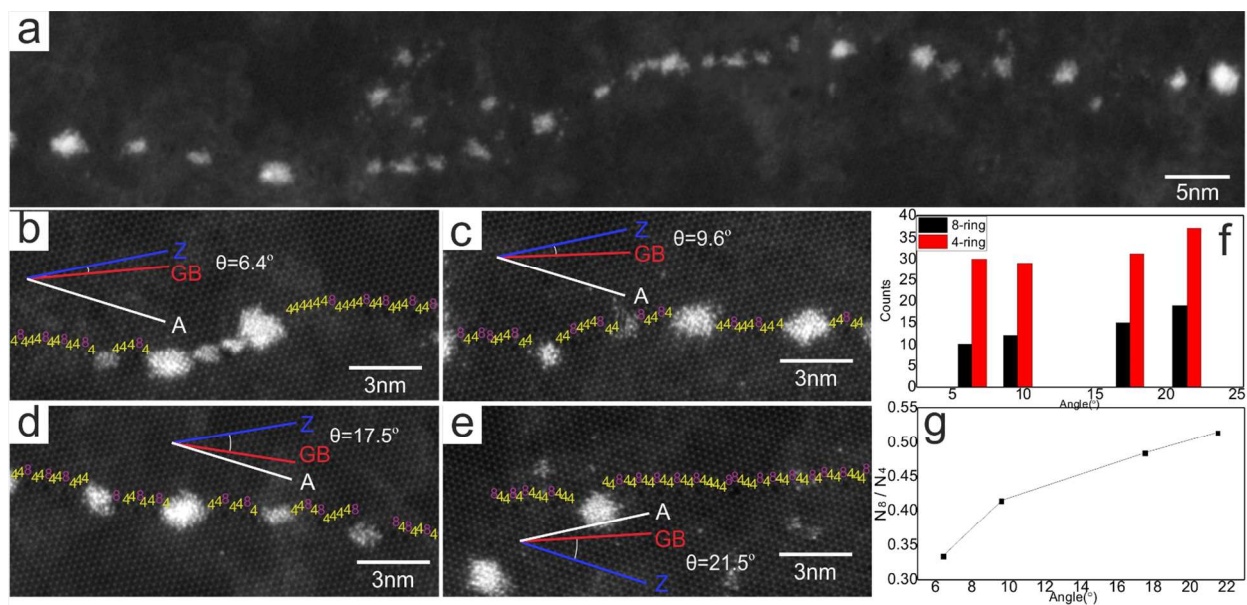

Figure 5. (a) ADF-STEM image of an antiphase GB in monolayer MoS_2, tracked by the Pt cluster decoration. Segments deviate from zigzag directions by an angle, θ between (b) 6.4°, (c) 9.6°, (d) 17.5°, (e) 21.5°. Specific directions (Z for zigzag, GB for propagation and A for armchair) are indicated. (f) Histogram of 4- and 8-member rings varying with θ. (g) ratio of 8-ring/4-ring in b-e as a function of θ.

We now discuss a possible growth process that could lead to antiphase GBs between multiple grains. Figure 6a shows an SEM image of MoS_2 grains with irregular shapes. The morphological irregularity is attributed to various factors including: growth temperature, presence of impurities, local Mo/S source concentration fluctuation and substrate effects. Two groups of grains, each of which contains three grains, are of particular interest. In each group, two grains sharing a common orientation exhibit a 60° rotation with respect to a third grain. Three grains can merge (as indicated in Figure 6) and a meandering antiphase GB forms at a certain stage of growth. These observations are consistent with the GB formation mechanism described by Huang et al.[53] Initially, a group of grains with S-terminated zigzag edges nucleate on a bare substrate (Figure 6b). The edges of each grain subsequently grow at uneven speeds and hence the grains show irregular morphologies (Figure 6c). Two grains with the same orientation then merge (Figure 6d) and continue to grow until they contact the 60° rotated grain (Figure 6e). As shown in Figure 6f, this mechanism gives rise to two segments of an antiphase GB with an angle of $\sim 95^o$ between the grains and a special 8-member ring at the apex that facilitates the large directional change of the antiphase GB.
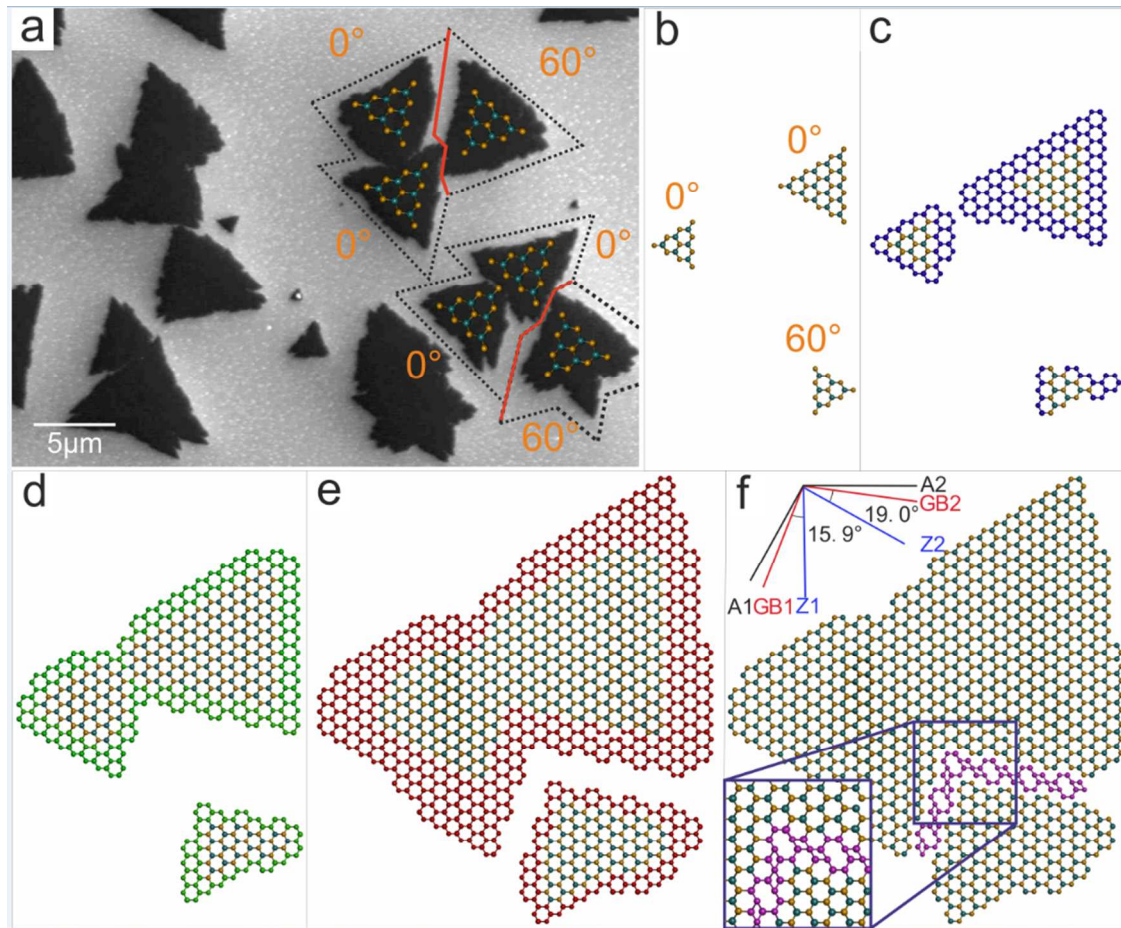
Figure 6. (a) SEM image showing the irregular shape of MoS_2 domains grown on a Si/Si_2O_3 wafer by CVD. Grains are superimposed with atomic structures to indicate orientation differences. Angles shown are relative to the reference domain in each group. The meandering antiphase GBs formed by merging grains are highlighted by red. (b-f) Schematic atomic models illustrating the growth process of two antiphase GBs with a turning angle of ~95° which are connected by one 8-member ring at the apex.

Figure 7a shows the top side part of Figure 2h. Figure 7b shows magnified zone D where a large directional change of the antiphase GB occurs, similar to that proposed in figure 6. At this location two antiphase GB segments (GB1 and GB2) meet with a rotation angle of ~104°. Both segments show a similar tilt angle (21.5° and 22.5°) from their respective zigzag directions, indicating a negligible difference in the 8-member ring density. The meeting point of the antiphase GB is examined at the

atomic-level in Figure 7c and d, qualitatively matching the structure in Figure 7f. Figures 7e-g compare the 8-member ring at the turning point to those in the other sections of the GB. Mo atoms in the alternative positions (Mo1 and Mo3 or Mo2 and Mo4) connect 4-member rings along the same zigzag directions, whereas neighboring Mo atoms (Mo1 and Mo4) at the meeting point facilitate directional switching from Z1 to Z2. Figures 7h-j show how the change in angle of the antiphase GB influences the same bilayer domain by examining zones C, F and E. Zone C, which is associated with GB1 direction has the 2H:3R change (figure 7h), and the 3R stacking is maintained all the way to zone F (figure 7i), but at zone E (associated with GB2 direction), we see a reversal of the stacking from 3R:2H (figure 7j). However, Figure 7k shows a region at the zone G, within the bilayer where the antiphase GB has another sharp turn and this induces local 2H-3R-2H changes. The 3R section in the middle, figure 7k, has blurred lattice contrast, indicating poor lattice registration within the 3R stacking, which is due to the competing strain effects of the GBs in different directions.
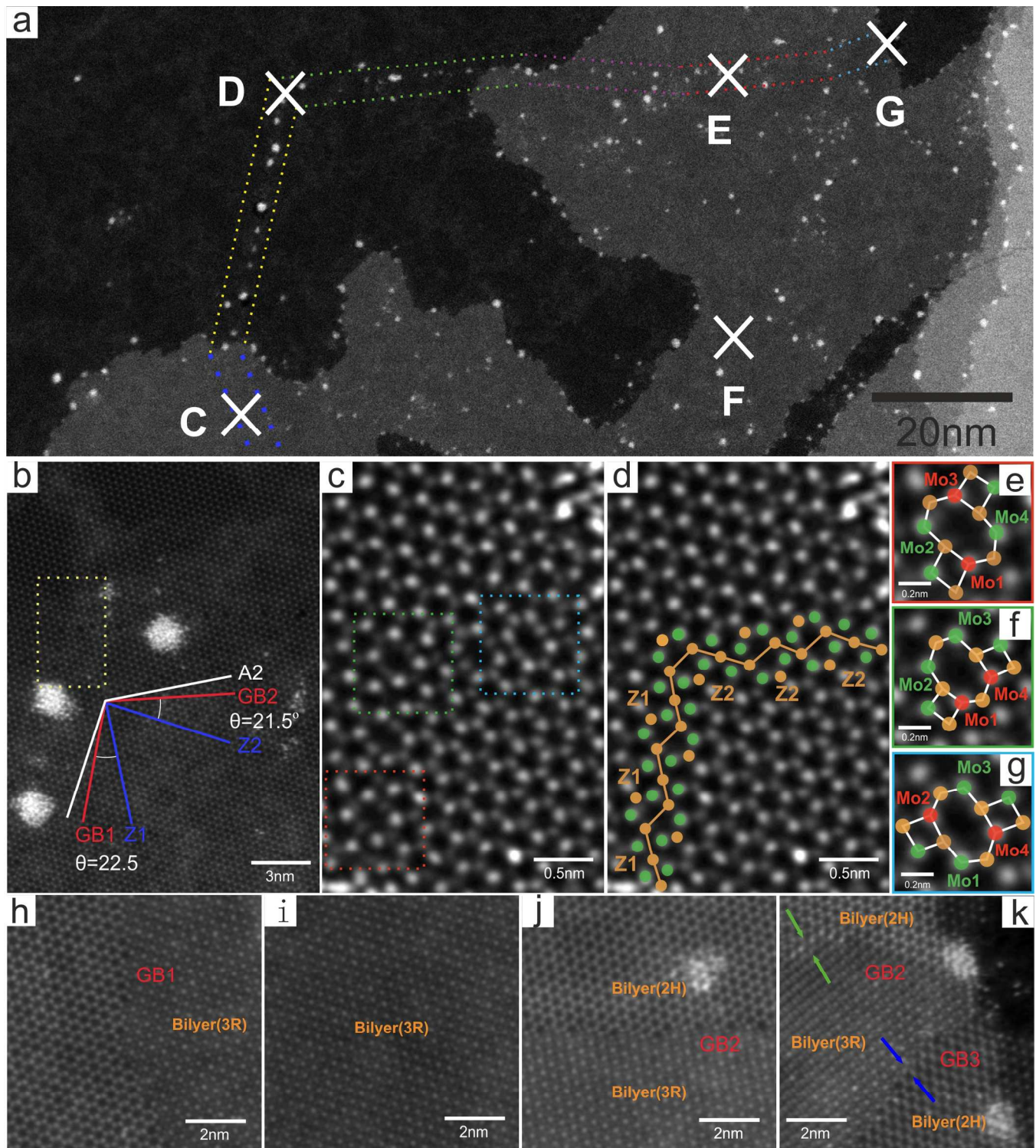
Figure 7. (a) Low magnification image showing the top-side part in figure 2h. (b) ADF-STEM image showing large turning angle for an antiphase GB. Armchair (A1 and A2), zigzag (Z1 and Z2) and propagation directions (GB1 and GB2) are marked in white, blue and red, respectively. (c) ADF-STEM image showing the apex of the

two antiphase GB directions. (d) Schematic illustration of the pathway of the antiphase GB superimposed on the ADF-STEM image in (b). (e-g) 8-member defects that enable GB kinks, superimposed with atomic structures. Images are taken from the boxed areas in (e) the left-hand side (f) the center and (g) the right-hand side of the apex of two antiphase GBs. (h-j) ADF-STEM images showing how the large GB turning angle impacts the bilayer 2H and 3R stacking from zones C, F and E. (k) Region at the end of zone E, where the GB takes another large turn and causes local stacking changes of 2H and 3R. Contraction directions described in the text are indicated by green and blue arrows.

Conclusion

We have demonstrated that the propagation of an anti-phase GB from a MoS_2 monolayer into a bilayer region causes atomically sharp stacking changes from 2H-3R, which is reversed upon a second antiphase GB crossing. Anti-phase GBs within the monolayer section can propagate with arbitrate direction by the combination of 4-fold and 8-fold rings, where the ratio depends upon GB angle relative to the zig-zag lattice direction of MoS_2. Large turning angles of the anti-phase GB were also observed and are mediated by a specific 8-member ring defect that has different positions of the attaching 4-member rings. Anti-phase GBs in the MoS_2 bilayer region exhibit larger lattice shrinkage along the Mo-Mo direction compared to the pure monolayers which is confirmed by DFT calculations. Overall, our data show that there is an energetic competition between a perfect 2H-3R stacking interface and in-plane bonding, in which interlayer van der Waals forces cause a bond contraction in MoS_2 due to antiphase GBs in order to achieve atomically sharp 2H-3R stacking sequences in the bilayer. These results provide a detailed characterization of antiphase GBs in monolayer MoS_2 and will help guide the understanding of their structure-property correlation. The observation of atomically sharp interface states may offer unique transport properties, given that topological confinement states can be created in 2D systems. Prior work has shown that graphene nanoroads in hBN sheets have 1D transport channels,[54] and that

spatial variation of the interlayer potential difference in bilayer graphene also gives rise to topologically protected 1D states.[55,56] Future work on the interfaces described in our manuscript here may also reveal such unique 1D confined states.

Methods

MoS_2 CVD synthesis and transfer

Synthesis of MoS_2 was carried out in two individually controlled quartz tube furnaces with Ar flowing at atmospheric pressure over S (1 g of purum grade >99.5%) and MoO_3 powders. The MoO_3 precursor was initially loaded in a 1 cm diameter tube, which was in turn placed inside the larger diameter 1 in. tube of the CVD furnace. This prevented cross-contamination of S and MoO_3 prior to MoS_2 formation on the target substrate, with the S separated in the larger diameter outer tube. Two furnaces were used to control the temperature of each precursor and the substrate, with heating temperatures for S=180 °C, MoO_3=300 °C, with the substrate held at 800 °C. Ar was used as a carrier gas. The S initially vaporized for 15 min, before the temperature of the second furnace was increased to 800 °C at 40 °C/min and left for 15 min under an Ar flow of 150 sccm. The Ar flow was then reduced to 10 sccm for 25 min, followed by a fast cooling (sample removal). The S temperature was kept at 180 °C throughout.

The as-grown sample was spin coated with a PMMA scaffold (8 wt% in anisole, 495k molecular weight) at 4700 rpm for 60 s and then cured at 150 °C for 15 min. The edge of the wafer was then ground with a diamond file to expose the SiO_2/Si edges to an etchant solution. The underlying SiO_2/Si substrate was detached by floating the sample on a 15 M KOH (Sigma-Aldrich) solution in a water bath for 2 h at 40 °C. The resultant suspended PMMA-MoS_2 film was thoroughly cleaned by several transfers to DI water. For the STEM characterization, the PMMA-MoS_2 film was transferred onto a holey Si_3N_4

grid and dried overnight in air. The PMMA-MoS$_2$-Si$_3$N$_4$ was finally baked at 150 $^{\circ}$C for 15 min to improve sample adhesion and the PMMA was subsequently removed using acetone for 24h.

Scanning Transmission Electron Microscopy

Room temperature ADF-STEM was performed using an aberration corrected JEOL ARM300CF STEM equipped with a JEOL ETA corrector[57] operated at an accelerating voltage of 60 kV located in the electron Physical Sciences Imaging Centre (ePSIC) at Diamond Light Source. The convergence semi-angle used was 24.6 mrad with a camera length of 20 cm, corresponding to an annular recording range of 39-156 mrad at the detector plane. The electron probe diameter was focused to ~72 pm with a dwell time ranging from 10-20 μs per pixel for imaging. The beam current was measured as 23 pA.

Image Simulations and Processing

Multislice ADF image simulations used the JEMS software package. ImageJ was used to process the ADF-STEM images. A bandpass filter (between 100 and 1 pixels) and a Gaussian blur (2 pixels) were applied to minimize the long-range effects in intensity due to uneven illumination.

Density Functional Theory (DFT) calculation

The DFT simulations were conducted using the Vienna Ab initio Simulation Package.[58] The Perdew-Burke-Ernzerhof exchange-correlational functional,[59] and the projector augmented wave method were employed in our calculations.[60] DFT calculations of both monolayer and bilayer MoS$_2$ systems (consisting of 180 and 360 atoms, respectively) were performed. A vacuum layer of 10 Å was included to reflect the 2D nature of the material. A plane wave basis set with an energy cutoff of 300 eV was adopted to expand the electronic wave functions. The Brillouin zone integration was conducted on a $1 \times 27 \times 2$ Monkhorst-Pack k-point mesh,[61] and the atomic coordinates in all structures were relaxed until the maximum residual force was below 0.02 eV $\cdot$ Å^{-1}.

Acknowledgements

References

(1)   Gong, Y.; Lin, J.; Wang, X.; Shi, G.; Lei, S.; Lin, Z.; Zou, X.; Ye, G.; Vajtai, R.; Yakobson, B. I.; *et al*. Vertical and In-plane Heterostructures from WS_2/MoS_2 Monolayers. *Nat. Mater.* **2014**, *13*, 1135-1142.

(2)   Plechinger, G.; Nagler, P.; Kraus, J.; Paradiso, N.; Strunk, C.; Schüller, C. and Korn, T. Identification of Excitons, Trions and Biexcitons in Single-layer WS_2. *Physica status solidi (RRL)-Rapid Research Letters*. **2015**, *9*, 457-461.

(3)   Withers, F.; Bointon, T. H.; Hudson, D. C.; Craciun, M. F.; Russo, S. Electron Transport of WS_2 Transistors in a Hexagonal Boron Nitride Dielectric Environment. *Sci. Rep.* **2014**, *4*, 4967.

(4)   Sorkin, V.; Pan, H.; Shi, H.; Quek, S. Y.; Zhang, Y. W. Nanoscale Transition Metal Dichalcogenides: Structures, Properties, and Applications. *Crit. Rev. Solid State Mater. Sci.* **2014**, *39*, 319-367.

(5)   Komsa, H.-P.; Kotakoski, J.; Kurasch, S.; Lehtinen, O.; Kaiser, U.; Krasheninnikov, A. V. Two-Dimensional Transition Metal Dichalcogenides under Electron Irradiation: Defect Production and Doping. *Phys. Rev. Letts.* **2012**, *109*, 1-5.

(6)   Wang, Q. H.; Kalantar-Zadeh, K.; Kis, A.; Coleman, J. N.; Strano, M. S. Electronics and Optoelectronics of Two-Dimensional Transition Metal Dichalcogenides. *Nat. Nanotechnol.* **2012**, *7*, 699-712.

(7)   Ma, Y.; Dai, Y.; Guo, M.; Niu, C.; Lu, J.; Huang, B. Electronic and Magnetic Properties of Perfect, Vacancy-Doped, and Nonmetal Adsorbed $MoSe_2$, $MoTe_2$ and WS_2 Monolayers. *Phys. Chem. Chem. Phys.* **2011**, *13*, 15546-15553.

(8)   Lee, Y.H.; Zhang, X.Q.; Zhang, W.; Chang, M.T.; Lin, C.T.; Chang, K.D.; Yu, Y.C.; Wang, J.T.W.; Chang, C.S.; Li, L.J. and Lin, T.W. Synthesis of Large-area MoS_2 Atomic Layers with Chemical Vapor Deposition. *Advanced Materials*. **2012**, *24(17)*, 2320-2325.

(9)   Zhan, Y.; Liu, Z.; Najmaei, S.; Ajayan, P. M.; Lou, J. Large-area Vapor-phase Growth and Characterization of MoS_2 Atomic Aayers on a SiO_2 Substrate. *Small*. **2012**, *8(7)*, 966-971

(10)   Liu, K.K.; Zhang, W.; Lee, Y.H.; Lin, Y.C.; Chang, M.T.; Su, C.Y.; Chang, C.S.; Li, H.; Shi, Y.; Zhang, H.; Lai, C.S. Growth of Large-area and Highly Crystalline MoS_2 Thin Layers on Insulating Substrates. *Nano Letts*. **2012**, *12(3),* 1538-1544.

(11)   Shi, Y.; Zhou, W.; Lu, A.Y.; Fang, W.; Lee, Y.H.; Hsu, A.L.; Kim, S.M.; Kim, K.K.; Yang, H.Y.; Li, L.J.; J.C. Van der Waals Epitaxy of MoS_2 Layers Using Graphene as Growth Templates. *Nano Letts*. **2012**, *12(6)*, 2784-2791

(12)   Radisavljevic, B.; Radenovic, A.; Brivio, J.; Giacometti, I.V.; Kis, A. Single-layer MoS_2 Transistors. *Nat. Nanotechnol*. **2011**, *6(3)*, 147-150.

(13)   Dean, C.R.; Young, A.F.; Meric, I.; Lee, C.; Wang, L.; Sorgenfrei, S.; Watanabe, K.; Taniguchi, T.; Kim, P.; Shepard, K.L.; Hone, J. Boron Nitride Substrates for high-quality Graphene Electronics. *Nat. Nanotechnol*. **2010**, *5(10)*, 722-726.

(14)   Britnell, L.; Gorbachev, R.V.; Jalil, R.; Belle, B.D.; Schedin, F.; Mishchenko, A.; Georgiou, T.; Katsnelson, M.I.; Eaves, L.; Morozov, S.V.; Peres, N.M.R. Field-effect Tunneling Transistor based on Vertical Graphene Heterostructures. *Science*. **2012**, *335(6071)*, 947-950.

(15)   Mak, K.F.; Lee, C.; Hone, J.; Shan, J.; Heinz, T.F. Atomically Thin MoS_2: A New Direct-gap Semiconductor. *Phys. Rev. Letts*. **2010**, *105(13)*, 136805.

(16)   Yin, Z.; Li, H.; Li, H.; Jiang, L.; Shi, Y.; Sun, Y.; Lu, G.; Zhang, Q.; Chen, X.; Zhang, H. Single-Layer MoS_2 Phototransistors. *ACS Nano*. **2011**, *6(1)*, 74-80.

(17)   Yu, Q.; Jauregui, L.A.; Wu, W.; Colby, R.; Tian, J.; Su, Z.; Cao, H.; Liu, Z.; Pandey, D.; Wei, D.; Chung, T.F. Control and Characterization of Individual Grains and Grain Boundaries in Graphene Grown by Chemical Vapour Deposition. *Nat. Mater*. **2011**, *10(6)*, 443-449.

(18)   Wood, J.D.; Schmucker, S.W.; Lyons, A.S.; Pop, E.; Lyding, J.W. Effects of Polycrystalline Cu Substrate on Graphene Growth by Chemical Vapor Deposition. *Nano Letts*. **2011**, *11(11)*, 4547-4554.

(19)   Biró, L.P; Lambin, P. Grain Boundaries in Graphene Grown by Chemical Vapor Deposition. *New J. Phys*. **2013**, *15(3),* 035024.

(20)   Hilgenkamp, H.; Mannhart, J. Grain Boundaries in High-T Superconductors. *Rev Mod. Phys*. **2002**, *74(2),* 485.

(21)   Pande, C.S.; Cooper, K.P. Nanomechanics of Hall–Petch Relationship in Nanocrystalline Materials. *Prog. Mat. Sci*. **2009**, *54(6),* 689-706.

(22)   Ovidko, I. Review on Grain Boundaries in Graphene. Curved Poly-and nanocrystalline Graphene Structures as New Carbon Allotropes. *Rev. Adv. Mater. Sci.* **2012**, *30(3),* 201-224.

(23)   Zhao, L.; Rim, K.T.; Zhou, H.; He, R.; Heinz, T.F.; Pinczuk, A.; Flynn, G.W.; Pasupathy, A.N. Influence of Copper Crystal Surface on the CVD Growth of Large Area Monolayer Graphene. *Solid State Comm.* **2011**, *151(7),* 509-513.

(24)   Malola, S.; Häkkinen, H.; Koskinen, P. Structural, Chemical, and Dynamical Trends in Graphene Grain Boundaries. *Phys. Rev. B.* **2010**, *81(16),* 165447.

(25)   Cockayne, E.; Rutter, G.M.; Guisinger, N.P.; Crain, J.N.; First, P.N.; Stroscio, J.A. Grain Boundary Loops in Graphene. *Phys. Rev. B.* **2011**, *83(19),* 195425.

(26)   Kim, K. S.; Zhao, Y.; Jang, H.; Lee, S. Y.; Kim, J. M.; Kim, K. S.; Ahn, J. H.; Kim, P.; Choi, J. Y.; Hong, B. H. Large-Scale Pattern Growth of Graphene Films for Stretchable Transparent Electrodes. *Nature* **2009**, *457*, 706-710.

(27)   Reina, A.; Jia, X.; Ho, J.; Nezich, D.; Son, H.; Bulovic, V.; Dresselhaus, M. S.; Kong, J. Large Area, Few-Layer Graphene Films on Arbitrary Substrates by Chemical Vapor Deposition. *Nano Letts.* **2009**, *9*, 30-35.

(28)   Li, X.; Cai, W.; An, J.; Kim, S.; Nah, J.; Yang, D.; Piner, R.; Velamakanni, A.; Jung, I.; Tutuc, E.; et al. Large-AreaSynthesis of High-Quality and Uniform Graphene Films on Copper Foils. *Science* **2009**, *324*, 1312-1314.

(29)   Bae, S.; Kim, H. K.; Lee, Y.; Xu, X.; Park, J. S.; Zheng, Y.; Balakrishnan, J.; Lei, T.; Kim, H. R.; Song, Y. I.; et al. Roll-to-Roll Production of 30-Inch Graphene Films for Transparent Electrodes. *Nat. Nanotechnol.* **2010**, *5*, 574-578.

(30)   Cai, W.; Moore, A. L.; Zhu, Y.; Li, X.; Chen, S.; Shi, L.; Ruoff, R. S. Thermal Transport in Suspended and Supported Monolayer Graphene Grown by Chemical Vapor Deposition. *Nano Letts.* **2010**, *10*, 1645-1651.

(31)   Grantab, R.; Shenoy, V. B.; Ruoff, R. S. Anomalous Strength Characteristics of Tilt Grain Boundaries in Graphene. *Science* **2010**, *330*, 946-948.

(32)   Yazyev, O. V.; Louie, S. G. Electronic Transport in Polycrystalline Graphene. *Nat. Mater.* **2010**, *9*, 806-809.

(33)   Novoselov, K. S.; Jiang, D.; Schedin, F.; Booth, T. J.; Khotkevich, V. V.; Morozov, S. V.; Geim, A. K. Two-Dimensional Atomic Crystals. *Proc. Natl. Acad. Sci. U.S.A.* **2005**,*102*, 10451-10453.

(34)   Enyashin, A. N.; Bar-Sadan, M.; Houben, L.; Seifert, G. Line Defects in Molybdenum Disulfide Layers. *J. Phys. Chem. C* **2013**, *117*, 10842-10848.

(35) Qiu, H.; Xu, T.; Wang, Z.; Ren, W.; Nan, H.; Ni, Z.; Chen, Q.; Yuan, S.; Miao, F.; Song, F.; et al. Hopping Transport Through Defect-Induced Localized States in Molybdenum Disulphide. *Nat. Commun.* **2013**, *4*, 2442.

(36) Van Der Zande, A.M.; Huang, P.Y.; Chenet, D.A.; Berkelbach, T.C.; You, Y.; Lee, G.H.; Heinz, T.F.; Reichman, D.R.; Muller, D.A.; Hone, J.C. Grains and Grain boundaries in Highly Crystalline Monolayer Molybdenum Disulphide. *Nat. Mater.* **2013**, *12(6),* 554-561.

(37) Zhou, W.; Zou, X.; Najmaei, S.; Liu, Z.; Shi, Y.; Kong, J.; Lou, J.; Ajayan, P.M.; Yakobson, B.I; Idrobo, J.C. Intrinsic Structural Defects in Monolayer Molybdenum Disulfide. *Nano Letts*. **2013**, *13(6),* 2615-2622.

(38) Zou, X.; Liu, Y.; Yakobson, B.I. Predicting Dislocations and Grain Boundaries in Two-Dimensional Metal-Disulfides from the First Principles. *Nano Letts.* **2012**, *13(1)*, 253-258.

(39) Lin, J.; Pantelides, S.T.; Zhou, W. Vacancy-Induced Formation and Growth of Inversion Domains in Transition-Metal Dichalcogenide Monolayer. *ACS Nano*. **2015**, *9(5)*, 5189-5197.

(40) Azizi, A.; Zou, X.; Ercius, P.; Zhang, Z.; Elías, A.L.; Perea-López, N.; Stone, G.; Terrones, M.; Yakobson, B.I.; Alem, N. Dislocation Motion and Grain Boundary Migration in Two-Dimensional Tungsten Disulphide. *Nat. Commun.* **2014**, *5*, 4867.

(41) Ly, T.H.; Perello, D.J.; Zhao, J.; Deng, Q.; Kim, H.; Han, G.H.; Chae, S.H.; Jeong, H.Y.; Lee, Y.H. Misorientation-Angle-Dependent *Nat. Commun.* **2016**, *7*, 10426.

(42) Liu, X.; Balla, I.; Bergeron, H.; Hersam, M.C. Point Defects and Grain Boundaries in Rotationally Commensurate MoS$_2$ on Epitaxial Graphene. *The J. Phys. Chem. C*. **2016,** *120(37),* 20798-20805.

(43) Najmaei, S.; Liu, Z.; Zhou, W.; Zou, X.; Shi, G.; Lei, S.; Yakobson, B. I.; Idrobo, J.-C.; Ajayan, P. M.; Lou, J. Vapour Phase Growth and Grain Boundary Structure of Molybdenum Disulphide Atomic Layers. *Nat. Mater.* **2013**, *12*, 754-759.

(44) Najmaei, S.; Amani, M.; Chin, M. L.; Liu, Z.; Birdwell, A. G.; O'Regan, T. P.; Ajayan, P. M.; Dubey, M.; Lou, J. Electrical Transport Properties of Polycrystalline Monolayer Molybdenum Disulfide. *ACS Nano* **2014**, *8*, 7930-7937.

(45) Guo, W.; Wu, B.; Li, Y.; Wang, L.; Chen, J.; Chen, B.; Zhang, Z.; Peng, L.; Wang, S.; Liu, Y. Governing Rule for Dynamic Formation of Grain Boundaries in Grown Graphene. *ACS Nano*. **2015**, *9(6)*, 5792-5798.

(46) Elibol, K.; Susi, T.; Maria, O.; Bayer, B.C.; Pennycook, T.J.; McEvoy, N.; Duesberg, G.S.; Meyer, J.C.; Kotakoski, J. Grain Boundary-Mediated Nanopores in Molybdenum Fisulfide Grown by Chemical Vapor Deposition. *Nanoscale.* **2017**, *9,* 1591-1598.

(47)   Bayer, B. C.; Caneva, S.; Pennycook, T. J.; Kotakoski, J.; Mangler, C.; Hofmann, S.; Meyer, J. C.; Introducing Overlapping Grain Boundaries in Chemical Vapour Deposited Hexagonal Boron Nitride Monolayer Films, *ACS Nano*, **2017**, 11, 4521-4527

(48)   Zhao, X.; Ding, Z.; Chen, J.; Dan, J.; Poh, S. M.; Fu, W.; Pennycook, S. J.; Zhou, W.; Loh, K. P.; Strain Modulation by van der Waals Coupling in Bilayer Transition Metal Dichalcogenide, *ACS Nano*, **2018**, 12, 1940-1948.

(49)   Zhou, S.; Wang, S.; Li, H.; Xu, W.; Gong, C.; Grossman, J.C.; Warner, J.H. Atomic Structure and Dynamics of Defects in 2D MoS_2 Bilayers. *ACS Omega*. **2017**, *2(7),* 3315-3324.

(50)   Rong, W.; He, K.; Pacios, M.; Robertson, A. W.; Bhaskaran, H.; Warner, J. H.; Controlled Preferential Oxidation of Grain Boundaries in Monolayer Tungsten Disulfide for Direction Optical Imaging, ACS Nano, **2015**, 9, 3695-3703

(51)   Wang, S.; Sawada, H.; Han, X.; Zhou, S.; Li, S.; Guo, Z. X.; Kirkland, A. I.; Warner, J. H.; Preferential Pt Nanocluster Seeding at Grain Boundary Dislocations in Polycrystalline Monolayer MoS2, ACS Nano, 2018, 12, 5626-5636

(52)   Lahiri, J.; Lin, Y.; Bozkurt, P.; Oleynik, I.I.; Batzill, M. An Extended Defect in Graphene as a Metallic Wire. *Nat. Nanotechnol*. **2010**, *5,* 326-329.

(53)   Huang, P.Y.; Ruiz-Vargas, C.S.; van der Zande, A.M.; Whitney, W.S.; Levendorf, M.P.; Kevek, J.W.; Garg, S.; Alden, J.S.; Hustedt, C.J.; Zhu, Y.; Park, J. Grains and Grain Boundaries in Single-Layer Graphene Atomic Patchwork Quilts. *Nature.* **2011**, *469(7330),* 389-392.

(54)   Jung, J.; Qiao, Z.; Niu, Q.; MacDonald, A. H.; Transport Properties of Graphene Nanoroads in Boron Nitride Sheets, Nano Lett., 2012, 12, 2936-2940

(55)   Qiao, Z.; Jung, J.; Niu, Q.; MacDonald, A. H.; Electronic Highways in Bilayer Graphene, Nano Lett. 2011, 11, 3453-3459

(56)   Martin, I.; Blanter, Y. M.; Morpurgo, A. F.; Topological Confinement in Bilayer Graphene, Phys. Rev. Lett., 2008, 100, 036804

(57)   Hosokawa, F.; Sawada, H.; Kondo, Y.; Takayanagi, K.; Suenaga, K. Development of Cs and Cc Correctors for Transmission Electron Microscopy. Microscopy 2013, 62, 23-41.

(58)   Kresse, G.; Furthmüller, J. Efficient Iterative Schemes for ab initio Total-Energy Calculations Using a Plane-Wave Basis set. Phys. Rev. B. 1996, 54, 11169-11186.

(59)   Perdew, J. P.; Burke, K.; Ernzerhof, M. Generalized Gradient Approximation Made Simple. *Phys. Rev. Lett.* **1996**, *77,* 3865-3868.

(60)   Blöchl, P. E. Projector Augmented-wave Method. *Phys. Rev. B.* **1994**, *50,* 17953-17979.

(61)   Monkhorst, H. J.; Pack, J. D. Special Points for Brillouin-Zone Integrations. *Phys. Rev. B.* **1976**, *13,* 5188-5192.

TOC Graphic